REPORT DOCUMENTATION PAGE

Form Approved
OMB No. 0704-0188

1. REPORT DATE *(DD-MM-YYYY)* 15-11-2010	2. REPORT TYPE Technical	3. DATES COVERED *(From - To)* 01-05-2009 01-11-2010

4. TITLE AND SUBTITLE

MEASUREMENT OF RUBIDIUM NUMBER DENSITY
UNDER OPTICALLY THICK CONDITIONS

5a. CONTRACT NUMBER
FA7000-10-2-0023

5b. GRANT NUMBER
USAFA-BAA-2009-1

5c. PROGRAM ELEMENT NUMBER

6. AUTHOR(S)
Matthew D. Rotondaro, Ph.D.

Lt Col Charles Wisniewski
Gordon Hager, Ph. D.

5d. PROJECT NUMBER

5e. TASK NUMBER

5f. WORK UNIT NUMBER

7. PERFORMING ORGANIZATION NAME(S) AND ADDRESS(ES)
U.S. Air Force Academy, Department of Aeronautical Engineering
2410 Faculty Drive
USAF Academy, 80840

8. PERFORMING ORGANIZATION REPORT NUMBER

9. SPONSORING / MONITORING AGENCY NAME(S) AND ADDRESS(ES)
High Energy Laser
Joint Technology Office
801 University Boulevard SE
Suite 209
Albuquerque NM, 87106

10. SPONSOR/MONITOR'S ACRONYM(S)
HEL-JTO

11. SPONSOR/MONITOR'S REPORT NUMBER(S)

12. DISTRIBUTION / AVAILABILITY STATEMENT
Distribution statement A. Approved for public release; distribution is unlimited.

13. SUPPLEMENTARY NOTES

14. ABSTRACT
A measurement of rubidium number density under optically thick conditions has been demonstrated by measuring the wings of the D_1 absorption spectra using a laser with a 0.16 nm (75 GHz) fine tuning range. This technique can measure the absolute concentration in rubidium under conditions where the absorption coefficient and path length product yield conditions where the central region of the line is opaque. The laser was tuned to a region sufficiently far into the short wavelength wing of the absorption where transmission through the cell was possible. The laser was then scanned through the central opaque region of the line to the adjacent long wavelength wing. The wavelength of the scan was calibrated by using a 1.5 GHz etalon and a cell containing only naturally occurring rubidium as a frequency reference. The measured absorption spectra for various cell conditions of temperature and pressure were then fit to a pressure broadened Voigt profile thereby allowing the determination of the rubidium number density.

15. SUBJECT TERMS
Rubidium, Heat Pipe, Number Density, Spectroscopy

16. SECURITY CLASSIFICATION OF: U			17. LIMITATION OF ABSTRACT	18. NUMBER OF PAGES	19a. NAME OF RESPONSIBLE PERSON Matthew Rotondaro
a. REPORT U	**b. ABSTRACT** U	**c. THIS PAGE** U	UU	22	**19b. TELEPHONE NUMBER** *(include area code)* (719) 333-9078

Standard Form 298 (Rev. 8-98)
Prescribed by ANSI Std. Z39.18

MEASUREMENT OF RUBIDIUM NUMBER DENSITY UNDER OPTICALLY THICK CONDITIONS

M. ROTONDARO, PH.D., LT COL C. WISNIEWSKI, AND G. HAGER, PH.D.

Abstract. A measurement of rubidium number density under optically thick conditions has been demonstrated by measuring the wings of the D_1 absorption spectra using a laser with a 0.16 nm (75 GHz) fine tuning range. This technique can measure the absolute concentration in rubidium under conditions where the absorption coefficient and path length product yield conditions where the central region of the line is opaque. The laser was tuned to a region sufficiently far into the short wavelength wing of the absorption where transmission through the cell was possible. The laser was then scanned through the central opaque region of the line to the adjacent long wavelength wing. The wavelength of the scan was calibrated by using a 1.5 GHz etalon and a cell containing only naturally occurring rubidium as a frequency reference. The measured absorption spectra for various cell conditions of temperature and pressure were then fit to a pressure broadened Voigt profile thereby allowing the determination of the rubidium number density.

1. Background

In recent years, alkali metals have garnered a great deal of interest as a laser medium. The small energy defect between the D_1 and D_2 lines make potassium, rubidium and caesium excellent candidates for efficient, high-power laser systems. While these alkali metals offer great promise, there are several issues which need to be resolved. Two such issues are heat dissipation and the challenge of holding the alkali number density constant during laser operation. This work will make inroads into both of these issues.

The first issue is maintaining a constant alkali metal concentration during operation. The ability to maintain constant alkali metal concentration is dependent on the ability to measure the concentration. This measurement, while in principle is not difficult, is extremely difficult

1

under the optically thick conditions at which an alkali metal laser operates. The measurement of the concentration is performed by scanning a laser across the D_1 or D_2 line and measuring the absorption [9]. Once this absorption spectra is measured then equation 1.1 can be applied to relate the observed spectra to the number density N. The measured spectra is a direct measurement of $\frac{I(\nu)}{I_0}$ where $\sigma(\nu)$ is the absorption cross-section and L is the length of the cell.

$$(1.1) \qquad \ln\left(\frac{I(\nu)}{I_0}\right) = -N\sigma(\nu)L$$

Under conditions favorable for the operation of an alkali laser the number density of the alkali metal is sufficiently high to render the cell opaque at line center. This issue, in principle, can be circumvented by starting a laser scan in a wing, scanning through the opaque region and then capturing the wing on the other side of the peak. These peak fragments can then be fit using a highly constrained fitting function thereby reconstructing the spectra. While this is possible at low pressures at high pressure where the line becomes significantly broad this becomes even more difficult. An alkali laser requires a high pressure of buffer gas to induce spin-orbit relaxation of the D_2 to D_1 line. The buffer gas also has the effect of broadening the lines. Therefore, to accomplish a wing to wing laser scan the laser must have a tuning range on the order of 75 GHz with a step size in the range of 0.5 GHz. Fortunately, a laser is available that can scan such a broad region and will be employed to make these concentration measurements.

The second issue is the heat dissipation resulting from the spin orbit relaxation of the D_2 excited state to the D_1 upper laser level. This heat deposition along the laser path increases the temperature of the alkali metal and buffer gas in the laser gain region. This has the effect of degrading the laser performance [5]. To date, the actual mechanism for this performance drop-off has not been determined. With the ability to measure alkali metal concentration under conditions favorable for alkali metal laser operation it will be possible to probe the gain media and make a determination as to the cause of this performance degradation.

2. Experimental Setup

The experimental apparatus is depicted in figure 1 and a list of the components can be found in table 1 Starting at the laser, the broadband tunable laser source is routed through three beam splitters and into an etalon. The first beam splitter directs the laser beam into the sample heat pipe. This beam splitter is situated upon a translation stage along

with it's paired detector to facilitate radial dependent number density measurements in the heat pipe. The heat pipe was enclosed in a heat block and a set of cold blocks. Heat blocks of various lengths were constructed to facilitate the heating of different lengths of the heat pipe. By adjusting the heated region this effectively set the length of the heat pipe. The heat blocks were heated using standard resistive heating and the cold blocks were cooled using a refrigerated water circulator. The pressure and composition of the diluent within the heat pipe could also be adjusted using the attached gas handling system. The gas handling system consisted of a vacuum pump, 10 Torr and 1000 Torr baratrons, various valves and a line going to a regulated gas cylinder. The second beam-path was directed into a second heat pipe. This heat pipe contained only naturally occurring rubidium. This second heat pipe was used as an absolute wavelength reference. The third beam-path monitored the laser power throughout each scan. This was absolutely necessary due to the large changes in laser power during a scan. The final path is to an etalon. This etalon was used to linearize the scan axis and to establish the correct spacing between each data point. The axis was then shifted to the correct wavelength using the rubidium wavelength reference.
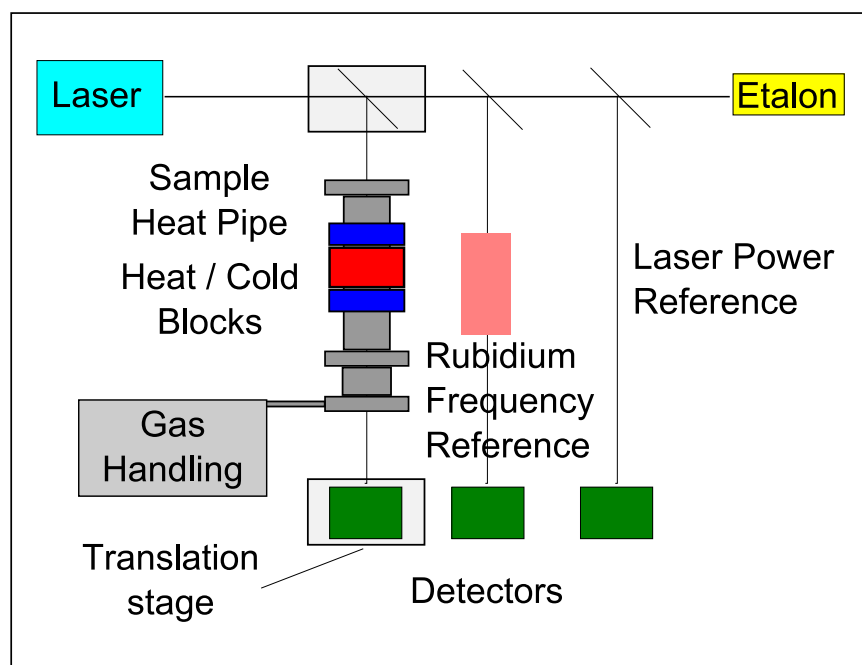

FIGURE 1. Experimental apparatus

Item	Manufacturer	Model
Tunable Laser (794-804nm)	New Focus	Velocity 6314
Detectors (400-1070nm)	New Focus	2031
Spectrum Analyzer	Coherent	240
Beam Splitters	Melles Griot	BBS-485-529-1025-45
Items Not Depicted		
Lock-in Amplifiers	Stanford Research	SR850
Variable Neutral Density Filter	Melles Griot	CNDQ-2-2.00
Refrigerated Water Circulator	Thermo Scientific	RTE7
Vacuum Pump	Cole-Parmer	79203-30
Baratrons	MKS	102A, 690A

TABLE 1. Apparatus equipment list

The temperature of each heat pipe was monitored using a thermocouple set in the heat block such that its sensor was situated just below the bottom of the heat pipe. This sensor allowed course control of the heat pipe temperature and allowed monitoring such that the temperature of the heat pipes could be held constant during data acquisition runs. Although, these temperature measurements did not represent a true measure of the temperature of the alkali metal. This discrepancy is attributed to the thermal conductivity of the heat pipe casing and the hot / cold regions surrounding the probe region induced by the heat / cold blocks respectively.

The data was acquired using two lock-in amplifiers. The two most important measurement were the laser power and the sample cell therefore, these were acquired using the phase averaging inputs of the lock-ins. The rubidium reference, and the etalon were also acquired using the lock-ins but these were recorded using the auxiliary inputs. All data was saved in its raw format to allow post processing of the data.

The laser has a large tuning region (794-804 nm) which can be scanned, using the stepper motor, in increments as small as 0.01 nm (4.75 GHz). This step size is too coarse for the purpose of measuring the pressure broadening and therefore the number density. Subsequently, it was necessary to use the fine frequency scan mode of the laser which employs a piezoelectric crystal. The piezoelectric crystal position as a function of input voltage can be seen if figure 2. Additionally, the discrete nature of the piezoelectric crystals steps can be seen in the blown-up region on the figure. The piezoelectric crystal voltage could be set between 3.8% and 99.8% of maximum in increments of 0.4%.

The fine region scan length is 0.16 nm (75G Hz) therefore, the minimum fine scan step size is approximately 0.67 pm (315 MHz). This scan size and the finesse of the etalon put a limit on the highest resolution etalon that could be used because of the necessity to access all etalon resonance peaks. Therefore, a (1.5 GHz) etalon was chosen as a wavelength reference.
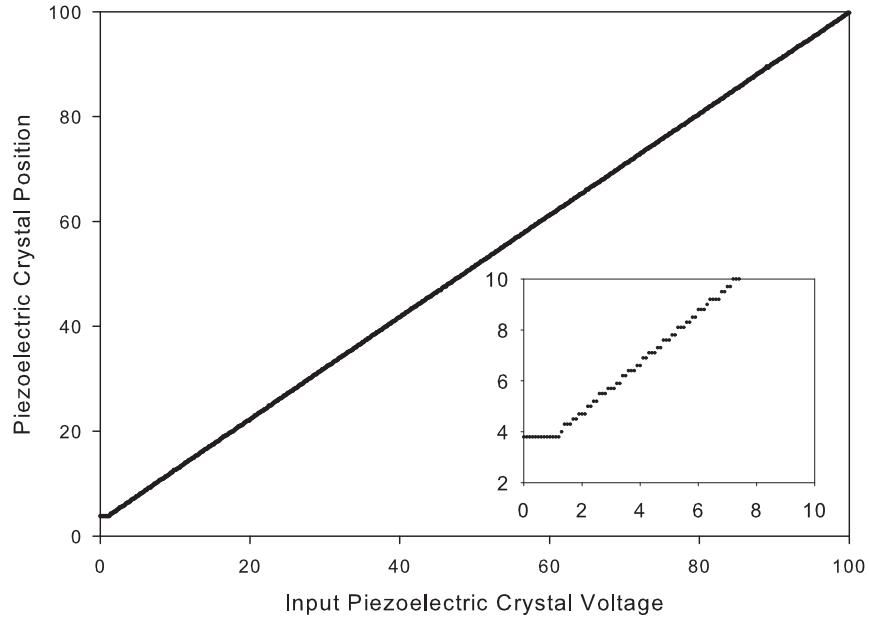

FIGURE 2. Piezoelectric crystal position as a function of the input voltage to the crystal. The emphasized region indicates the discrete nature of the piezoelectric crystals steps.

3. DATA ACQUISITION

In preparation for taking data, the first step was to ensure the heat pipes were set to the appropriate temperature. For the sample heat pipe, this meant waiting a sufficient length of time for the temperature of the heat block to fully stabilize. For the reference cell, this meant ensuring there was a sufficiently strong absorption spectra to ensure a good quality fit later in the analysis.

During the warmup period for the heat pipes, the laser was set to its initial scanning position. This was accomplished by setting the initial

wavelength of the laser to a sufficiently low wavelength to ensure it was well outside of any of the absorption features. Then the piezoelectric crystal was set to 50% of its range. Then, the laser was scanned slowly, using the laser's stepper motor on its smallest step size, towards longer wavelengths until the reference cell absorption spectra began to appear on the data acquisition monitor. At that point the laser's course scan was stopped. This placed the laser at the center of the absorption feature. The laser could then be scanned from 0-100% of the piezoelectric crystal range allowing the acquisition of the absorption spectra. The laser can't really scan from 0-100% it is actually limited to 3.8-99.8%. By inverting the data represented in figure 2 and fitting the result to a line. It is possible to improve the linearity of the scan. The resulting fit is given in equation 3.1.

$$(3.1) \qquad\qquad V_{Act} = 1.03067 V_{Des} - 3.013635$$

Where V_{Act} is the actual voltage sent to the piezoelectric crystal and V_{Des} is the desired voltage setting. V_{Des} can range from 3.8-99.8%. This correction to the laser scan is not really necessary because any nonlinearity in the scan will be corrected using the data from the etalon. The reason for the application of this correction is to reduce the difficulty of fitting the etalon data.

When the laser is scanned four channels of data are collected. These channels are the signal from the sample cell, rubidium reference cell, laser power and the etalon. The data was acquired using two lock-in amplifiers. The two most important measurement were the laser power and the sample cell. The laser power because all other measurements were ratioed against it to correct for the laser's power fluctuations during the scan. The sample cell because it is the data used to measure the rubidium number density. Therefore, these were acquired using the phase averaging inputs of the lock-in amplifiers. The rubidium reference, and the etalon were also acquired using the lock-in amplifiers but these were recorded using the auxiliary inputs. All data was saved in its raw format to allow post processing of the data. Typical raw data can be seen in figure 3. As can be seen, the laser power has a large variation over the entire scan region. This fluctuation is corrected by ratioing all of the collected data by the laser power. The ratioed data can be seen in figure 4. This data represents $-\ln(\frac{I_{Sample}}{I_0})$, $-\ln(\frac{I_{Ref}}{I_0})$ and $\frac{I_{Etalon}}{I_0}$. As can be seen the fluctuations in the laser power are corrected.
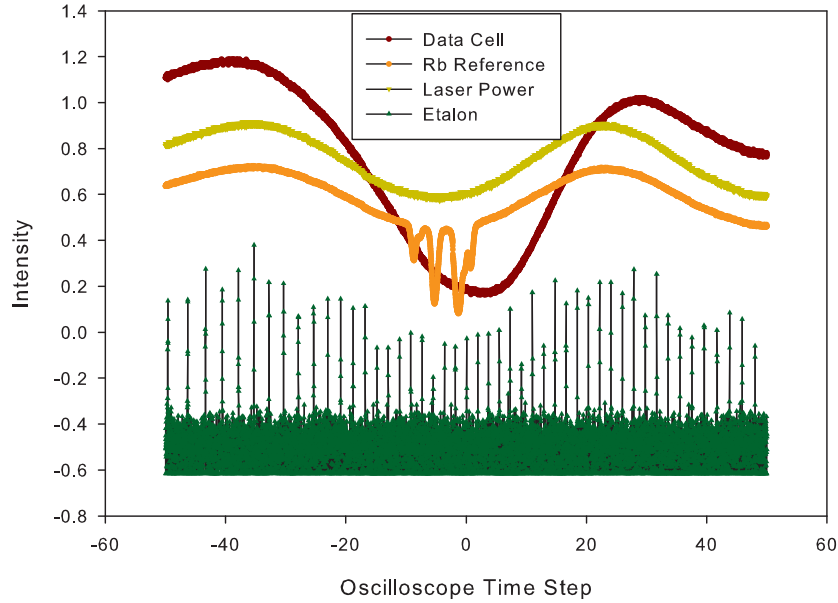
FIGURE 3. Typical raw data

The X-axis of the collected data represents the divisions used by the data acquisition equipment and needs to be converted into a wavelength. This is accomplished by using the etalon data. The procedure for using the etalong data is explained it detail in [7] but to summarize. The etalon data is fit using the software package PeakFit Version 4.12. This software is very good at finding the peak center of a long line of successive peaks. It is critical that the software identify every peak. Once each peak is identified, an X-Y table is created using the peak centers as the X values and the incremental spacing of each peak as determined by the etalon spacing for the Y values. Once this table is created it is then fit to a third degree polynomial. This polynomial is then used to correct for any nonlinearity and to set the correct spacing between adjacent points. This results in an x-axis that has the correct wavelength spacing but has not been shifted to the correct wavelength. This correction is applied to both the sample cell data and the rubidium reference cell data.

The next step is to shift the x-axis to the correct wavelength. This is accomplished by fitting the rubidium reference data to a series of Gaussian curves. The gaussian line shape is chosen because the rubidium is dominated by Doppler broadening which results in a Gaussian
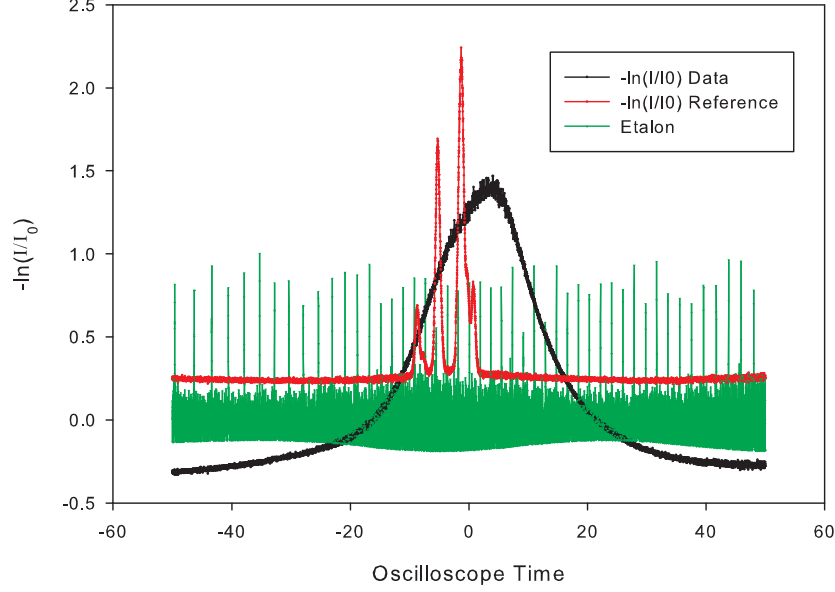
FIGURE 4. Data that has been divided by the laser power

line shape. The relative spacing and line strengths of the rubidium lines has been well documented [10] [11] and the exact D_1 line shape $g(\lambda)$ or $g(\nu)$ can be reconstructed using equations 3.2 or 3.3

$$(3.2) \qquad g(\lambda) = \sum_{F,F',iso} f_F f_{iso} S_{FF'} * g_{Gauss}(\lambda, \lambda_{FF'})$$

$$(3.3) \qquad g(\nu) = \sum_{F,F',iso} f_F f_{iso} S_{FF'} * g_{Gauss}(\nu, \nu_{FF'})$$

Where the Gaussian in both wavelength and frequency are given by equations 3.4 and 3.5.

$$(3.4) \quad g_{Gauss}(\lambda, \lambda_{FF'}) = \sqrt{\frac{4\ln(2)}{\pi}} \frac{1}{\Delta\lambda_D} \exp\left[-4\ln(2)\left(\frac{\lambda - \lambda_{FF'}}{\Delta\lambda_D}\right)^2\right]$$

$$(3.5) \quad g_{Gauss}(\nu, \nu_{FF'}) = \sqrt{\frac{4\ln(2)}{\pi}} \frac{1}{\Delta\nu_D} \exp\left[-4\ln(2)\left(\frac{\nu - \nu_{FF'}}{\Delta\nu_D}\right)^2\right]$$

The two forms of the line shape are related by equation 3.6

$$(3.6) \qquad g_{Gauss}(\lambda, \lambda_{FF'}) = \frac{\lambda^2}{c} g_{Gauss}(\nu, \nu_{FF'})$$

and both are normalized when integrated over all frequencies as shown by equations 3.7.

$$(3.7) \qquad \int_0^\infty g_{Gauss}(\lambda, \lambda_{FF'})d\lambda = \int_0^\infty g_{Gauss}(\nu, \nu_{FF'})d\nu = 1$$

The full width at half maximum (FWHM) for each form is given in equation 3.8.

$$(3.8) \qquad \Delta\lambda_D = \lambda_0\sqrt{\frac{8kT\ln(2)}{Mc^2}}, \Delta\nu_D = \nu_0\sqrt{\frac{8kT\ln(2)}{Mc^2}}$$

Where k is the Boltzmann constant, T is the temperature, M is the mass of a rubidium atom and c is the speed of light.

In the previous equations, F is the hyperfine quantum number of the starting level and F' is the hyperfine quantum number of the ending level. f_F is the statistical distribution of the F state and is given by equation 3.9.

$$(3.9) \qquad f_F = \frac{(2F+1)e^{-E(F)/kT}}{\sum_F(2F+1)e^{-E(F)/kT}} \approx \frac{(2F+1)}{\sum_F(2F+1)}$$

This approximation is allowed because the energy E(F) is very small representing the energy defect between the hyperfine split levels. Examining the worst case, the hyperfine splitting of the ground state, $exp(\frac{-E(F)}{kT}) \simeq 0.999$. The isotopic abundance is represented by f_{iso} and is 0.2783 for Rubidium 87 and 0.7217 for Rubidium 85. The product $S_{FF'} * f_F$ is given in table 3. $S_{FF'}$ is the relative hyperfine transition strength factors given in table 2. $\lambda_{FF'}$ is the line center of the transition F to F'.

Rb 87				Rb 85			
S_{11}	1/6	S_{12}	5/6	S_{22}	2/9	S_{23}	7/9
S_{21}	1/2	S_{22}	1/2	S_{32}	5/9	S_{33}	4/9

TABLE 2. Relative hyperfine transition strength factors $S_{FF'}$

Rb 87				Rb 85			
$S_{11}f_1$	1/16	$S_{12}f_1$	5/16	$S_{22}f_2$	10/108	$S_{23}f_2$	35/108
$S_{21}f_2$	5/16	$S_{22}f_2$	5/16	$S_{32}f_3$	35/108	$S_{33}f_3$	28/108

TABLE 3. Relative hyperfine transition strength factors multiplied by the statistical distribution of the hyperfine levels. $S_{FF'} * f_F$

The line centers $\lambda_{FF'}$ are determined by calculating the line positions relative to the $S_{\frac{1}{2}}$(F=2) to $P_{\frac{1}{2}}$(F=2) transition in ^{87}Rb and $S_{\frac{1}{2}}$(F=3) to $P_{\frac{1}{2}}$(F=2) transition in ^{85}Rb for the D_1 line.

The total energy of a hyperfine split level with the total angular momentum F is given by equation 3.10 from reference [6].

$$(3.10) \qquad E_F = E_J + A\frac{C}{2} + B\frac{\frac{3}{4}C(C+1) - I(I+1)J(J+1)}{2I(2I-1)J(2J-1)}$$

with

$$
\begin{aligned}
C &= F(F+1) - I(I+1) - J(J+1); \\
F &= I+J, I+J-1, ... |I-J|; \\
A &= \frac{\mu_I \overline{H(0)}}{IJ}; \\
B &= eQ\overline{\phi_{JJ}(0)}.
\end{aligned}
$$

E_J is the fine structure energy, and the hyperfine splitting is given by the last two terms. The term $A\frac{C}{2}$ represents the splitting due to the nuclear magnetic moment which is dependent upon the magnetic moment μ_I, the magnetic field produced by the nucleus $\overline{H(0)}$ and the product of the quantum numbers IJ which represents the coupling of the angular momentum vectors through the magnetic interaction where $I = \frac{3}{2}$ for ^{87}Rb and $I = \frac{5}{2}$ for ^{85}Rb. The last term represents the quadrupole interaction which depends on Q, the quadrupole moment, $\overline{\phi_{JJ}(0)}$, the vector gradient of the electric field of the orbital electrons having cylindrical symmetry about the J axis evaluated at the nucleus, and e is the absolute value of the elementary charge.

The relative line positions are given in Table 4. The first half of the table provides the A and B spectroscopic constants which can be used to determine the relative line positions as in Figure 5. The figure accurately represents the relative line positions within each manifold but the spacing between manifolds is not to scale. The relative line positions are computed in the second half of Table 4 using equation 3.11.

$$(3.11) \qquad rp_{FF'} = \frac{\lambda_0^2}{c}\left[\left(E_F^{5^2P_J} - E_F^{5^2S_{\frac{1}{2}}}\right) - \left(E_{F'}^{5^2P_J} - E_{F'}^{5^2S_{\frac{1}{2}}}\right)\right]$$

All line positions are reported relative to the $S_{\frac{1}{2}}(F=2)$ to $P_{\frac{1}{2}}(F=2)$ transition in ^{87}Rb for the D_1 line and to the $S_{\frac{1}{2}}(F=2)$ to $P_{\frac{3}{2}}(F=3)$ transition in ^{87}Rb for the D_2 line. The ^{85}Rb shifts are relative to the $S_{\frac{1}{2}}(F=3)$ to $P_{\frac{1}{2}}(F=2)$ transition for the D_1 line and to the $S_{\frac{1}{2}}(F=3)$

	^{87}Rb Ref [1] [2] [3] [4] [12]		^{85}Rb Ref [1] [2] [3]	
MHz	A	B	A	B
$5^2S_{\frac{1}{2}}$	3417.341305452145(45)	-	1011.9108130(20)	-
$5^2P_{\frac{1}{2}}$	407.24(77)	-	120.527(56)	-
$5^2P_{\frac{3}{2}}$	84.7185(20)	12.4965(37)	25.0020(99)	25.790(93)

rp_i		^{87}Rb			^{85}Rb	
nm	F	1	2	F	2	3
$P_{\frac{1}{2}}$	1	-0.0126821	0.0017159	2	-0.0063951	0
	2	-0.014398	0	3	-0.0071568	-0.0007617
$P_{\frac{3}{2}}$	0	-0.013353	-	1	-0.006333	-
	1	-0.013506	0.000892	2	-0.006395	0
	2	-0.013836	0.000562	3	-0.006528	-0.0001335
	3	-	0	4	-	-0.0003877

GHz	F	1	2	F	2	3
$P_{\frac{1}{2}}$	1	6.02014	-0.81454	2	3.03573	0
	2	6.83468	0	3	3.39731	0.361581
$P_{\frac{3}{2}}$	0	6.33886	-	1	3.00636	-
	1	6.41109	-0.423592	2	3.03573	0
	2	6.56803	-0.266652	3	3.09913	0.06340
	3	-	0	4	-	0.18404

cm^{-1}	F	1	2	F	2	3
$P_{\frac{1}{2}}$	1	0.20081	-0.02717	2	0.10126	0
	2	0.22798	0	3	0.11332	0.01206
$P_{\frac{3}{2}}$	0	0.21144	-	1	0.10028	-
	1	0.21385	-0.014129	2	0.10126	0
	2	0.21908	-0.008894	3	0.10337	0.00211
	3	-	0	4	-	0.00614

TABLE 4. A and B coefficients and relative line positions, rp_i

to $P_{\frac{3}{2}}(F = 2)$ transition for the D_2 line. This requires an additional parameter, the spacing between the ^{87}Rb and the ^{85}Rb lines. This spacing has been calculated using the values reported in [10] [11] for the D_1 line as -0.0014843 nm (704.07 MHz) (0.023485 cm^{-1}) and for the D_2 line

FIGURE 5. Rubidium 85 and 87 5^2P hyperfine split levels.

as -0.0019138 nm (942.44 MHz) (0.031436 cm^{-1}). The absolute wavelength correction of the axis requires that these transitions be shifted to the absolute position of the $S_{\frac{1}{2}}(F = 2)$ to $P_{\frac{1}{2}}(F = 2)$ transition in ^{87}Rb which is 794.9836 nm (377.1059 THz) and for the $S_{\frac{1}{2}}(F = 2)$ to $P_{\frac{3}{2}}(F = 3)$ transition in ^{87}Rb it is 780.246 nm (384.228 THz). Once these values have been calculated the line shape can be assembled using equation 3.2 and this can be seen graphically in figure 6.

In order to extract the shift needed to correct the data's X-axis, this constructed line shape is assembled as a user function in the software package TableCurve 2D v5.01.01. The etalon corrected reference data
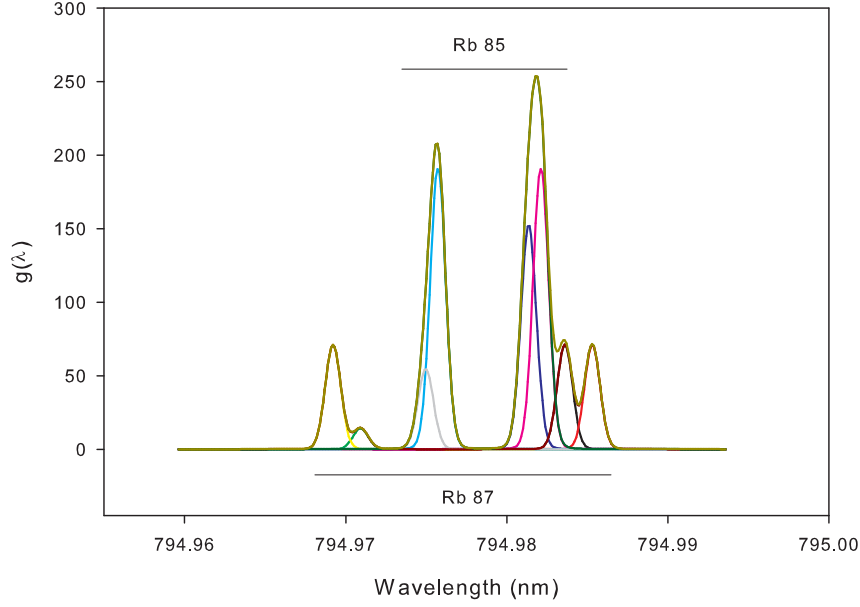
FIGURE 6. Natural rubidium with each D_1 hyperfine transition explicitly shown

is then fit allowing the extraction of the shift necessary to correct the wavelength axis and the Doppler width. Reference data with the its resulting curve fit are shown in figure 7. The Doppler width is used to determine the temperature of the rubidium within the heat pipe.

By using the fit of the etalon peaks and the fit from the rubidium reference, the data can be both scaled and shifted such that the x-axis represents the wavelength of the spectra. There is an additional step needed to correct the axis. The etalon is actually a spectrum analyzer therefore, one of it's mirrors is attached to a piezoelectric crystal. This crystal can move from the application of an external voltage or from changes in room temperature. Therefore, it is necessary to do a second set of fits on the data. The etalon peaks are fit and the resulting fit is applied to the reference data. The reference data is then fit allowing the x-axis to scale. The scale parameter, is then applied to the spacing of the etalon peaks and the etalon peak spacing is readjusted to account for this small correction. Then, the result is applied to both the reference cell and the sample cell data. The resulting reference data is then fit one final time to ensure the x-axis has been properly scaled and shifted. Data with the wavelength axis corrected is depicted in figure 8
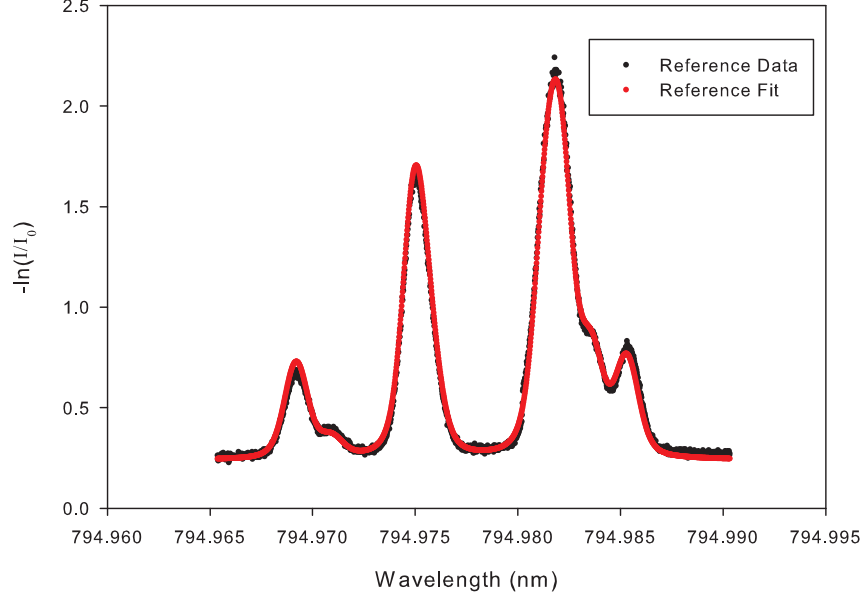
FIGURE 7. Rubidium 87 data with fits

4. DATA ANALYSIS

Once the data has been acquired and the wavelength axis has been scaled and shifted to the correct wavelength region it can be used to extract the rubidium number density. The sample heat pipe contained naturally occurring rubidium and was filled to various pressures ranging between 0 Torr and 1000 Torr using helium, nitrogen and ethane as diluent. Because of the addition of the diluent and the various pressure ranges, the spectra in the sample cells consisted of both a Gaussian line shape and a pressure broadened Lorentzian line shape. Therefore, the resulting line shape is composed of the sum eight Voigt profiles. A Voigt line shape is represented by equations 4.1 and 4.2.

(4.1)
$$g_{Voigt}(\lambda, \lambda_{FF'}) = \frac{1}{2\pi\sqrt{\pi}} \int_{-\infty}^{\infty} \left[\frac{\Delta\lambda_L \exp(-t^2)}{(\lambda - \lambda_{FF'} - t\frac{\Delta\lambda_D}{\sqrt{4\ln(2)}})^2 + (\frac{\Delta\lambda_L}{2})^2} \right] dt$$

(4.2)
$$g_{Voigt}(\nu, \nu_{FF'}) = \frac{1}{2\pi\sqrt{\pi}} \int_{-\infty}^{\infty} \left[\frac{\Delta\nu_L \exp(-t^2)}{(\nu - \nu_{FF'} - t\frac{\Delta\nu_D}{\sqrt{4\ln(2)}})^2 + (\frac{\Delta\nu_L}{2})^2} \right] dt$$
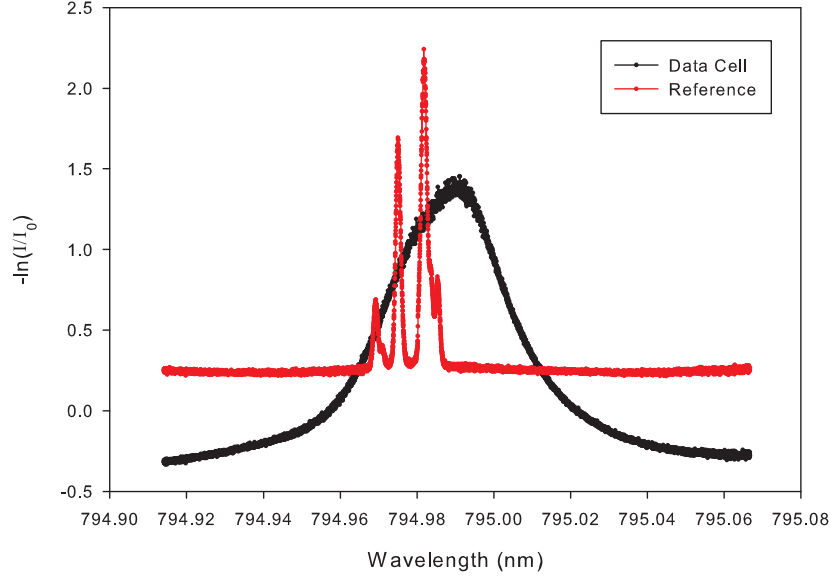
FIGURE 8. Data that has been scaled and shifted using the etalon and reference data

Using the Voigt line shape and equation 3.2 the line shape for the rubidium sample heat pipe spectra can be constructed. The resulting Voigt line shape can be curve fit to the data and the Voigt full width at half maximum (FWHM) and the amplitude can be obtained. This method works well when the entire rubidium spectra is observed but under highly opaque conditions the Voigt profile is quite difficult to fit. To improve the quality of the fit and subsequently the quality of the number density measurement, the Gaussian and the Lorentzian FWHM are calculated using equations 3.8 and 4.3 respectively.

$$(4.3) \qquad \Delta\lambda_L = R(\lambda)P, \Delta\nu_L = R(\nu)P$$

Where P is the pressure of the diluent and R is the broadening rate given in $\frac{MHz}{Torr}$ or $\frac{nm}{Torr}$. The Ethane value used for the broadening rate R was 27.8 $\frac{MHz}{Torr}$ measured at 314.15 K and it was obtained from [13]. The Helium value used for the broadening rate R was 18.90 $\frac{MHz}{Torr}$ measured at 394 K and it was obtained from [8].

The Doppler FWHM is temperature dependent and therefore can't be calculated without a precise measurement of the temperature. That temperature can be measured by measuring the Doppler width of the rubidium at 0 Torr of diluent. While the temperature may change as diluent is added to the heat pipe the $\sqrt{T}$ dependance of the doppler

width will vary slowly and therefore can be neglected. These FWHM values are then fixed and the only parameters that are allowed to float are the baseline and the amplitude of the Voigt profile. Typical data with their associated fits is depicted in figure 9.
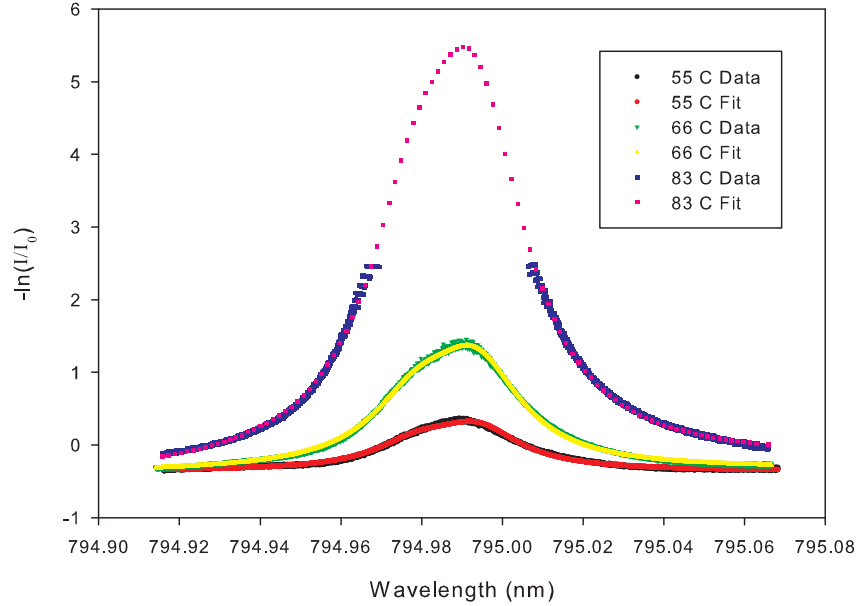

FIGURE 9. Rubidium 87 data with fits

Once the amplitude of the spectra is determined Beer's Law equation 1.1 and the relationship between the absorption cross section and the line shape equation 4.4 can be combined to for equations 4.9 and 4.10 which are used to calculate the number density. This analysis was conducted using wavelength as the X-axis therefore, the wavelength form of the equations were used. The frequency form of the equations were included for completeness. The results of these calculations can be seen in figure 10 also depicted is the number density calculation using the vapor pressure curve equation 4.11 from [10] which is reported to have an accuracy better than $\pm 5\%$. Note, this equation has been modified to yield number density N /m^3 as a function and temperature T in Kelvin.

(4.4)
$$\sigma(\nu) = \frac{\lambda^2}{8\pi\tau} g(\nu, \nu_{FF'}, \Delta\nu_D, \Delta\nu_L), \sigma(\lambda) = \frac{\lambda^4}{8\pi\tau c} g(\lambda, \lambda_{FF'}, \Delta\lambda_D, \Delta\lambda_L)$$

(4.5) $\quad -\ln\left(\frac{I(\nu)}{I_0(\nu)}\right) = N\sigma(\nu)L = NL\frac{\lambda^2}{8\pi\tau} g(\nu, \nu_{FF'}, \Delta\nu_D, \Delta\nu_L)$

(4.6) $\quad -\ln\left(\frac{I(\lambda)}{I_0(\lambda)}\right) = N\sigma(\lambda)L = NL\frac{\lambda^4}{8\pi\tau c} g(\lambda, \lambda_{FF'}, \Delta\lambda_D, \Delta\lambda_L)$

(4.7) $\quad A_{Fit}(\nu) g(\nu, \nu_{FF'}, \Delta\nu_D, \Delta\nu_L) = NL\frac{\lambda^2}{8\pi\tau} g(\nu, \nu_{FF'}, \Delta\nu_D, \Delta\nu_L)$

(4.8) $\quad A_{Fit}(\lambda) g(\lambda, \lambda_{FF'}, \Delta\lambda_D, \Delta\lambda_L) = NL\frac{\lambda^4}{8\pi\tau c} g(\lambda, \lambda_{FF'}, \Delta\lambda_D, \Delta\lambda_L)$

(4.9)
$$N = A_{Fit}(\nu)\frac{8\pi\tau}{L\lambda^2}$$

(4.10)
$$N = A_{Fit}(\lambda)\frac{8\pi\tau c}{L\lambda^4}$$

(4.11)
$$N = \frac{2.077 \times 10^9}{kT} \cdot 10^{\frac{-4040}{T}}$$

Note, $A_{Fit}(\nu)$ is in units of 1/time and $A_{Fit}(\lambda)$ is in units of length.

5. CONCLUSIONS

As can be seen from figure 10 there is very good agreement between the number density measured by directly probing the heat pipe when compared to the expected value derived from equation 4.11 using the temperature measured from the doppler line shape. The measurements at higher temperatures resulted in a larger temperature uncertainty because the rubidium vapor pressure was sufficiently high to render the cell opaque at line center of the hyperfine split spectra. Therefore, the 0 Torr buffer gas spectra was fit using peak fragments as the high temperature number densities are measured. This resulted in a greater temperature uncertainty. Even with this uncertainty, the number density measurement is accurate because of the weak temperature dependance and small contribution to the line shape of the Doppler portion of the Voigt.
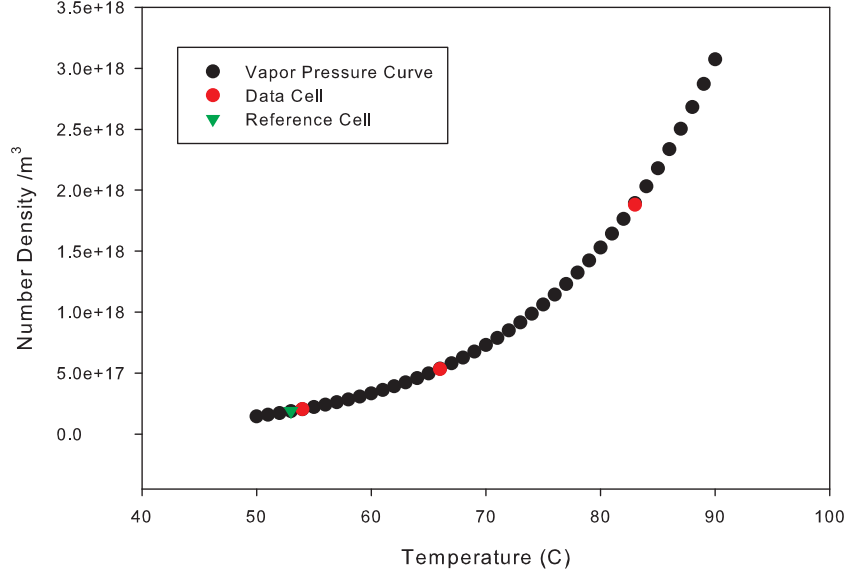
FIGURE 10. Measured rubidium number density as a function of temperature along with the vapor pressure curve for rubidium.

This methodology demonstrates a robust capability for measuring the number density of rubidium under conditions that are favorable for rubidium laser operation. Therefore, the application of this technique to diode pumped alkali metal lasers (DPAL) would yield valuable information that would enhance both our theoretical and experimental knowledge of DPAL systems.

6. APPENDIX 1

This is the curve fitting formalism used to perform the curve fits. This formalism develops the curve fit using an approximation of the Voigt profile. The actual curve fitting process used equation 6.1 which was integrated using an adaptive Gauss Quadrature.

(6.1)
$$V(\nu, \nu_{FF'}) = \alpha \frac{1}{2\pi\sqrt{\pi}} \int_{-\infty}^{\infty} \left[\frac{\Delta\nu_L \exp(-t^2)}{(\nu - \nu_{FF'} - \nu_s - t\frac{\Delta\nu_D}{\sqrt{4\ln(2)}})^2 + (\frac{\Delta\nu_L}{2})^2} \right] dt + b$$

$$(6.2) \quad G(\nu, \nu_{FF'}) = \alpha \sqrt{\frac{4\ln(2)}{\pi}} \frac{1}{\Delta\nu_D} \exp\left[-4\ln(2)\left(\frac{\nu - \nu_{FF'} - \nu_s}{\Delta\nu_D}\right)\right]$$

$$(6.3) \quad L(\nu, \nu_{FF'}) = \alpha \frac{\Delta\nu_L}{2\pi[(\frac{\Delta\nu_L}{2})^2 + (\nu - \nu_{FF'} - \nu_s)^2]}$$

$$(6.4) \quad U(\nu, \nu_{FF'}) = (1 - \eta)G(\nu, \nu_{FF'}) + \eta L(\nu, \nu_{FF'}) + b$$

$$(6.5) \quad \eta = \frac{a^2}{a^2 + l}$$

$$(6.6) \quad a = \frac{\Delta\nu_L}{\Delta\nu_D}, l = \frac{2}{1 + 0.0990\ln(2) + [(1 - 0.0990\ln(2))^2 + \frac{4\ln(2)}{a^2}]^{\frac{1}{2}}}$$

Nonlinear least squares fit

$$(6.7) \quad dA_{i,j} = \begin{bmatrix} \frac{\partial V}{\partial \alpha}|_{\nu_1} & \frac{\partial V}{\partial b}|_{\nu_1} & \frac{\partial U}{\partial \Delta\nu_L}|_{\nu_1} & \frac{\partial U}{\partial \Delta\nu_D}|_{\nu_1} & \frac{\partial U}{\partial \nu_s}|_{\nu_1} \\ \frac{\partial V}{\partial \alpha}|_{\nu_2} & \frac{\partial V}{\partial b}|_{\nu_2} & \frac{\partial U}{\partial \Delta\nu_L}|_{\nu_2} & \frac{\partial U}{\partial \Delta\nu_D}|_{\nu_2} & \frac{\partial U}{\partial \nu_s}|_{\nu_2} \\ \vdots & \vdots & \vdots & \vdots & \vdots \\ \frac{\partial V}{\partial \alpha}|_{\nu_m} & \frac{\partial V}{\partial b}|_{\nu_m} & \frac{\partial U}{\partial \Delta\nu_L}|_{\nu_m} & \frac{\partial U}{\partial \Delta\nu_D}|_{\nu_m} & \frac{\partial U}{\partial \nu_s}|_{\nu_m} \end{bmatrix}$$

$$(6.8) \quad dB_i = y_i - V(\nu; \alpha, b, \Delta\nu_L, \Delta\nu_D, \nu_s)$$

$$(6.9) \quad \mathbf{dA}^T\mathbf{dB} = (\mathbf{dA}^T\mathbf{dA})\mathbf{dX}$$

$$(6.10) \quad \mathbf{A} = \mathbf{dA}^T\mathbf{dA}, \mathbf{B} = \mathbf{dA}^T\mathbf{dB}$$

$$(6.11) \quad dX_i = \begin{bmatrix} d\alpha \\ db \\ d\Delta\nu_L \\ d\Delta\nu_D \\ d\nu_s \end{bmatrix}$$

Solved using the Jacobi Method

$$(6.12) \quad dX_i^{(k)} = \frac{B_i - \sum_{j\neq i} A_{i,j} dX_i^{(k-1)}}{A_{i,i}}$$

Iterate until done...

$$(6.13) \quad \frac{\partial V}{\partial \alpha} = \frac{1}{2\pi\sqrt{\pi}} \int_{-\infty}^{\infty} \left[\frac{\Delta\nu_L \exp(-t^2)}{(\nu - \nu_{FF'} - \nu_s - t\frac{\Delta\nu_D}{\sqrt{4\ln(2)}})^2 + (\frac{\Delta\nu_L}{2})^2} \right] dt$$

$$(6.14) \quad \frac{\partial V}{\partial b} = 1$$

$$(6.15) \quad \frac{\partial U}{\partial \Delta\nu_L} = \frac{2\alpha\eta(4(\nu_{FF'} + \nu_s - \nu)^2 - \Delta\nu_L{}^2)}{\pi(\Delta\nu_L{}^2 + 4(\nu_{FF'} + \nu_s - \nu)^2)^2}$$

(6.16)
$$\frac{\partial U}{\partial \Delta\nu_D} = \frac{2\alpha(\eta - 1)\ln(2)^{\frac{1}{2}} \left(\Delta\nu_D{}^2 - 8(\nu_{FF'} + \nu_s - \nu)^2 \ln(2) \right) \exp(-\frac{4(\nu_{FF'} + \nu_s - \nu)^2 \ln(2)}{\Delta\nu_D{}^2})}{\sqrt{\pi}\Delta\nu_D{}^4}$$

(6.17)
$$\frac{\partial U}{\partial \nu_s} = \frac{16\alpha(\nu - \nu_{FF'} - \nu_s)}{\pi} \left(\frac{\eta\Delta\nu_L}{\left(\Delta\nu_L{}^2 + 4(\nu_{FF'} + \nu_s - \nu)^2 \right)^2} - \frac{(\eta - 1)\ln(2)^{\frac{3}{2}}\sqrt{\pi} \exp(-\frac{4(\nu_{FF'} + \nu_s - \nu)^2 \ln(2)}{\Delta\nu_D{}^2})}{\Delta\nu_D{}^3} \right)$$
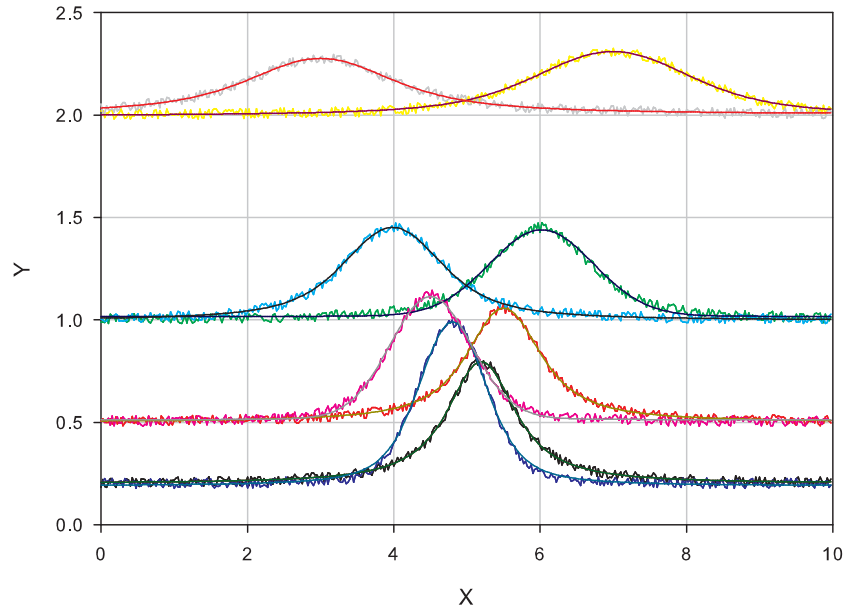

FIGURE 11. Need Text Here

A	b	$\Delta\nu_L$	$\Delta\nu_D$	ν_S
1	0.2	1	0.333	0.2
1.005	0.201	0.992	0.367	0.196
1	0.5	1	0.5	0.5
0.996	0.501	1.005	0.487	0.504
1	1	1	1	1
0.768	1.016	0.063	1.646	1.019
1	2	1	2	2
1.087	1.995	1.477	1.659	1.993
1	0.2	0.2	1	-0.2
1.138	0.189	0.519	0.793	-0.197
1	.5	.5	1	-.5
0.861	0.512	0.083	1.267	-0.497
1	1	1	1	-1
1.026	0.997	1.069	0.940	-1.015
1	2	2	1	-2
0.960	2.003	1.867	1.148	-2.002

TABLE 5. Comparison of Voigt parameters versus the values obtained from a fit.

REFERENCES

1. E. Arimondo, M. Inguscio, and P. Violino, *Experimental determinations of the hyperfine structure in the alkali atoms*, Reviews of Modern Physics **49** (1977), 31.
2. A. Banerjee, D. Das, and V. Natarajan, *Absolute frequency measurements of the D_1 lines in ^{39}K, ^{85}Rb and ^{87}Rb with ~ 0.1 ppb uncertainty*, Europhysics Letters **65** (2004), 172.
3. G.P. Barwood, P. Gill, and W.R.C. Rowley, *Frequency measurements on optically narrowed Rb-stabilised laser diodes at 780 nm and 795 nm*, Applied Physics B **53** (1991), 142.
4. S. Bize, Y. Sortais, M.S. Santos, C. Mandache, A. Clairon, and C. Salomon, *High-accuracy measurement of the ^{87}Rb ground-state hyperfine splitting in an atomic fountain*, Europhysics Letters **45** (1999), 558.
5. R.J. Knize, T. Ehrenreich, and B. Zhdanov, *Highly efficient scalable cesium vapor laser*, Journal of Directed Energy 2 (2006), 145–150.
6. Hans Kopfermann, *Nuclear moments*, New York: Academic Press INC., 1958.
7. Gerald C. Mankee, *Procedures for extracting temperature and concentrations from measured spectral lineshapes*, 2nd ed., Air Force Research Laboratory, Air Force Research Laboratory, Directed Energy Directorate, Kirtland AFB, NM, September 2003.
8. Matthew D. Rotondaro, *Collisional dynamics of the rubidium 5^2p levels*, Dissertation, Air Force Institute of Technology, 1995.

9. Matthew D. Rotondaro and Glen P. Perram, *Collisional broadening and shift of the rubidium D1 and D2 lines ($5^2S_{1/2} - 5^2P_{1/2}, 5^2P_{3/2}$) by rare gases, H2, D2, N2, CH4 and CF4*, Journal of Quantitative Spectroscopy and Radiative Transfer **57** (1997), 497.

10. Daniel A. Steck, *Rubidium 87 D line data*, vol. 2.1.1, Oregon Center for Optics and Department of Physics, University of Oregon, Department of Physics, 1274 University of Oregon, Eugene, Oregon 97403-1274, April 2009.

11. Daniel Adam Steck, *Rubidium 85 D line data*, vol. 0.2.1, Oregon Center for Optics and Department of Physics, University of Oregon, Department of Physics, 1274 University of Oregon, Eugene, Oregon 97403-1274, April 2009.

12. Jun Ye, Steve Swartz, Peter Jungner, and John L. Hall, *Hyperfine structure and absolute frequency of the ^{87}Rb $5P_{3/2}$ state*, Optics Leters **21** (1996), 1280.

13. Nathan D. Zameroski and Gordon D. Hager, *Pressure broadening and collisional shift of rubidium by CH4, C2H6, C3H8, NC4H10, He*, Unpublished, 2009.

2410 FACULTY DRIVE, USAF ACADEMY 80840